

A seismoacoustic study of the 2011 January 3 Circleville earthquake

Stephen J. Arrowsmith,¹ Relu Burlacu,² Kristine Pankow,² Brian Stump,³ Richard Stead,¹ Rod Whitaker¹ and Chris Hayward³

¹Los Alamos National Laboratory, NM, USA. E-mail: sarrowsmith@gmail.com

²University of Utah, UT, USA

³Southern Methodist University, TX, USA

Accepted 2012 February 10. Received 2012 February 9; in original form 2011 October 14

SUMMARY

We report on a unique set of infrasound observations from a single earthquake, the 2011 January 3 Circleville earthquake (M_w 4.7, depth of 8 km), which was recorded by nine infrasound arrays in Utah. Based on an analysis of the signal arrival times and backazimuths at each array, we find that the infrasound arrivals at six arrays can be associated to the same source and that the source location is consistent with the earthquake epicentre. Results of propagation modelling indicate that the lack of associated arrivals at the remaining three arrays is due to path effects. Based on these findings we form the working hypothesis that the infrasound is generated by body waves causing the epicentral region to pump the atmosphere, akin to a baffled piston. To test this hypothesis, we have developed a numerical seismoacoustic model to simulate the generation of epicentral infrasound from earthquakes. We model the generation of seismic waves using a 3-D finite difference algorithm that accounts for the earthquake moment tensor, source time function, depth and local geology. The resultant acceleration–time histories on a 2-D grid at the surface then provide the initial conditions for modelling the near-field infrasonic pressure wave using the Rayleigh integral. Finally, we propagate the near-field source pressure through the Ground-to-Space atmospheric model using a time-domain Parabolic Equation technique. By comparing the resultant predictions with the six epicentral infrasound observations from the 2011 January 3, Circleville earthquake, we show that the observations agree well with our predictions. The predicted and observed amplitudes are within a factor of 2 (on average, the synthetic amplitudes are a factor of 1.6 larger than the observed amplitudes). In addition, arrivals are predicted at all six arrays where signals are observed, and importantly not predicted at the remaining three arrays. Durations are typically predicted to within a factor of 2, and in some cases much better. These results suggest that measured infrasound from the Circleville earthquake is consistent with the generation of infrasound from body waves in the epicentral region.

Key words: Numerical approximations and analysis; Earthquake dynamics; Earthquake ground motions.

INTRODUCTION

Earthquakes are complex infrasonic sources and are thought to generate infrasound via a variety of mechanisms. The first such mechanism, referred to hereafter as epicentral infrasound, is associated with ground pumping in the epicentral region, and has been observed in a number of studies (Bolt 1964; Mikumo 1968; Young & Greene 1982; Mutschlecner & Whitaker 2005). The second mechanism, referred to in this paper as secondary infrasound, is associated with the passage of seismic surface waves through areas of extreme topography such as mountains or cliffs (Young & Greene 1982; Le Pichon *et al.* 2002, 2003, 2005; Arrowsmith *et al.* 2009a; Green *et al.* 2009). Finally, the third mechanism, which we refer to as local infrasound, is associated with the generation of infrasound from

vertical motion associated with seismic waves at the receiver array (Benioff & Gutenberg 1939; Bolt 1964; Donn & Posmentier 1964; Cook 1971; Kim *et al.* 2004).

A summary of recent measurements of infrasound from earthquakes (excluding observations of local infrasound) is shown in Fig. 1. These measurements make no distinction between epicentral and secondary sources; yet imply that, to first order, there exist linear relationships between earthquake magnitude and amplitude (normalized for distance) or signal duration. The scatter in these regressions is thought to be associated with variations in source properties (e.g. depth and mechanism), in addition to variations in path effects (e.g. near source geology, atmospheric winds and temperatures). The existing record of infrasound observations from earthquakes is not yet extensive enough, or detailed enough, to

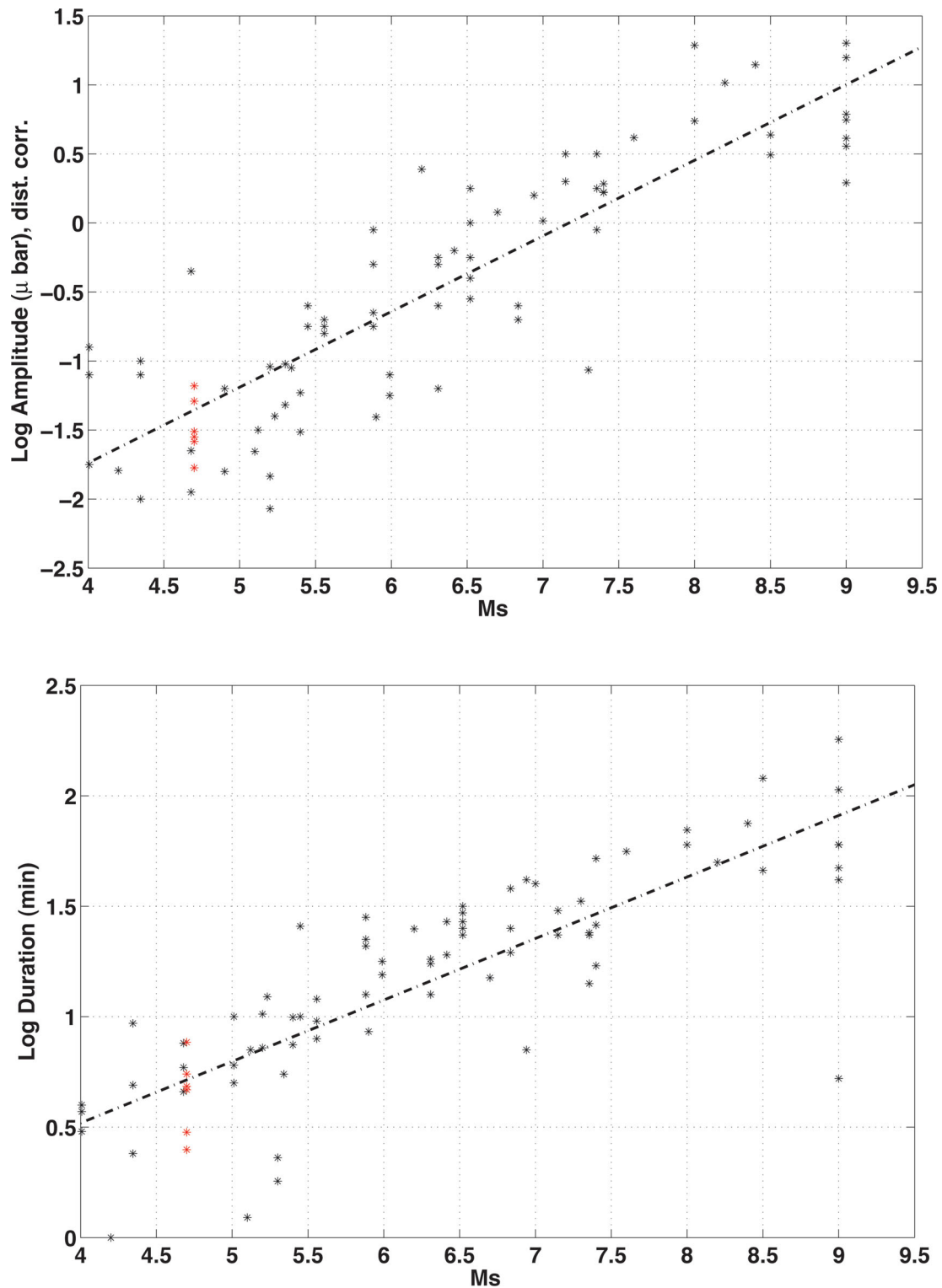


Figure 1. A synthesis of infrasound measurements from earthquakes to date (courtesy of Alexis Le Pichon), mainly comprising events from Mutschlechner & Whitaker (2005), below $M_s = 7.0$, showing that both amplitude and duration scale with magnitude. Black stars represent observations from previous studies; red stars represent this study. Distances are scaled to a reference distance of 1000 km. Magnitudes represent surface wave magnitudes (M_s). Much of the scatter is thought to be associated with additional source effects (e.g. depth, mechanism) in addition to path effects.

isolate these individual effects empirically. Thus, there is a need for improvements in the types and numbers of observations (primarily through the acquisition of spatially dense measurements) in addition to the development of numerical models that can allow us to explore these individual effects.

Beyond observational studies, models for secondary infrasound have been developed that agree well with observations for selected earthquakes (Le Pichon *et al.* 2003; Green *et al.* 2009). However, we are not aware of any previous attempt to model observations of epicentral infrasound, in part due to historically sparse networks of

acoustic arrays, which means that most observations of epicentral infrasound to date have been on single arrays. For robust association, evidence from a single array (which may comprise signal amplitude, duration, frequency, backazimuth and phase velocity) is not sufficient to uniquely associate a signal with a given event. This is evidenced by the continuing challenge faced by the IDC to reduce the number of false associations when combining seismic and infrasound catalogues and discussed further by Arrowsmith *et al.* (2008). Without a source location for the infrasound signals, it is difficult to isolate different types of earthquake infrasound (epicentral, secondary). We do not yet know enough about the characteristics of signals (e.g. amplitude, duration and frequency) generated by these different sources to confidently attribute them to one or the other source type.

In 2006 and 2007 (Stump *et al.* 2007), the first three of nine arrays that now compose the infrasound network in Utah were installed with the additional six installed in 2010. The multiple arrays provide sufficient spatial and temporal sampling of infrasound that is needed to better constrain and understand the generation of epicentral infrasound from earthquakes. The long-term goal being to improve upon the existing earthquake scaling laws shown graphically in Fig. 1. On 2011 January 3, an earthquake with M_w 4.7 occurred near the town of Circleville, Utah. The Circleville earthquake was recorded infrasonically at six of the nine arrays in the Utah infrasound network (Fig. 2). In this paper, we report on these unique observations, and on the subsequent development and validation of a numerical model for the generation of epicentral infrasound.

Seismic analysis

The Circleville earthquake was well recorded and described by the University of Utah Seismograph Stations (UUSS). The location was determined using traveltimes, a full moment tensor calculated using broad-band waveforms, and ground motion variations mapped using ShakeMap (Wald *et al.* 2003). The epicentral location ($38^\circ 14.84'N$ $112^\circ 20.39'W$) is well constrained. 95 per cent confidence intervals put the horizontal error at approximately ± 1 km. The depth (5.4 km) is less well constrained. The 95 per cent confidence interval is approximately ± 2.5 km. The larger depth error is expected, as the closest station is almost 27 km distant, much larger than the focal depth (Gomberg *et al.* 1990).

In addition to the location determined using traveltimes (given earlier), a full moment tensor was calculated (Whidden *et al.* 2011). The moment tensor calculation provides constraints on the moment magnitude (M_w 4.7), fault parameters (described later) and an independent depth estimate (8 km, slightly outside the 95 per cent confidence interval determined using traveltimes). To constrain the depth in the moment tensor calculation, the depth is fixed at 1 km increments between 2 and 25 km and the depth determined by the greatest variance reduction (VR) in waveform fit. Based on the VRs, the depth estimate from the moment tensor inversion is quite well constrained to be at a depth between 5 and 10 km with the greatest VR at 8 km, the preferred depth chosen for modelling. The fault parameters determined in this calculation indicate that the earthquake was primarily normal faulting on either a 67° southeast dipping plane or on a 35° west-dipping plane (Fig. 2). The southeast dipping plane (strike N45°E) is preferred and used in the modelling based on the regional structural trend, the more reasonable dip angle (67°) for a normal fault and the clustering of aftershocks to the east of the main shock (see Fig. 2 inset). Of note is that Hermann *et al.* (2011) determined the same 8 km depth (our preferred depth) and

similar moment tensor parameters using a different algorithm for the moment tensor calculation.

ShakeMap (Wald *et al.* 2003) is a tool developed to map observed and predicted horizontal ground motions. The ShakeMap for the Circleville earthquake is available at <http://quake.utah.edu/shake/00005268/intensity.html>. In generating the ShakeMap, a ground motion prediction equation for small earthquakes (Wald *et al.* 2003) was used together with site amplification factors (Borcherdt 1994) for the local geology to predict horizontal ground motion onto a uniform grid. The predicted horizontal ground motions are compared to the observed data and a bias between the observed and predicted ground motions is calculated. The bias to first order is a correction for errors in the magnitude, as it simply scales up or down the predicted ground motions. Neither the crustal velocity model nor the depth is a constraint to the ShakeMap. The only dependency on velocity is the average shear velocity in the upper 30 m (V_{s30}) used for site amplification calculations (see Borcherdt 1994). In Utah, V_{s30} is a function of the geological age of the mapped rocks (older rocks being faster than younger soil deposits). The depth is not a constraint because the ground motion prediction equation (Wald *et al.* 2003) uses the Joyner–Boore distance, which is defined as the closest horizontal distance to the vertical projection of the fault rupture on the Earth's surface (see Abrahamson & Shedlock 1997, their fig. 1). For small earthquakes (like Circleville), where the rupture plane has not been determined, the Joyner–Boore distance is approximated by the epicentral distance. This can result in slight overestimation of the calculated distances depending on the size and orientation of the rupture.

The calculated bias for the peak horizontal acceleration (PHA) is 0.7 for the Circleville earthquake. The closest station at a distance of 26 km recorded a PHA of ~ 1 per cent g . At the epicentre, ShakeMap predicts the PHA to be 8.7 per cent g . However, in modelling the infrasound, we are interested in the vertical motion. Unfortunately empirical peak ground motion relations and site amplification factors have only been developed for horizontal motions. In a comparison of measured PHA with the measured peak vertical acceleration (PZA) from the Circleville earthquake at the same station, we found that on average the PZA is ~ 85 per cent of the PHA for the seismic stations recording this event. However, there is significant scatter in the ratios, and for the modelling discussed later we choose a more conservative estimate of 75 per cent.

A unique seismoacoustic network

The UUSS has operated a regional seismic network for over four decades. Building on existing infrastructure and technical expertise, UUSS has integrated nine infrasonic arrays into its seismic network, with real-time telemetry for continuous data recording. The infrasonic arrays, with aperture of ~ 150 m, consist of four sensors for each array, with one of the elements colocated with a seismic station. Various sources capable of generating seismic and acoustic energy have been identified in the Utah region including mining explosions, rocket motor detonations and earthquakes. The focus on investigating infrasound generated by small earthquakes influenced the current spatial distribution of the infrasonic arrays in Utah, tracking the seismicity of the region (see Fig. 2). The infrasonic arrays are equipped with microphones (Chaparral 2, Chaparral 2.5 or IML ST models) fitted with 8 or 10 hoses, for noise reduction. Dataloggers (REFTEK 130,¹ Quanterra Q330²) are used to digitize data at 100 sps.

¹ REFTEK, Plano, TX, USA.

² Kinemetrics, Pasadena, CA, USA.

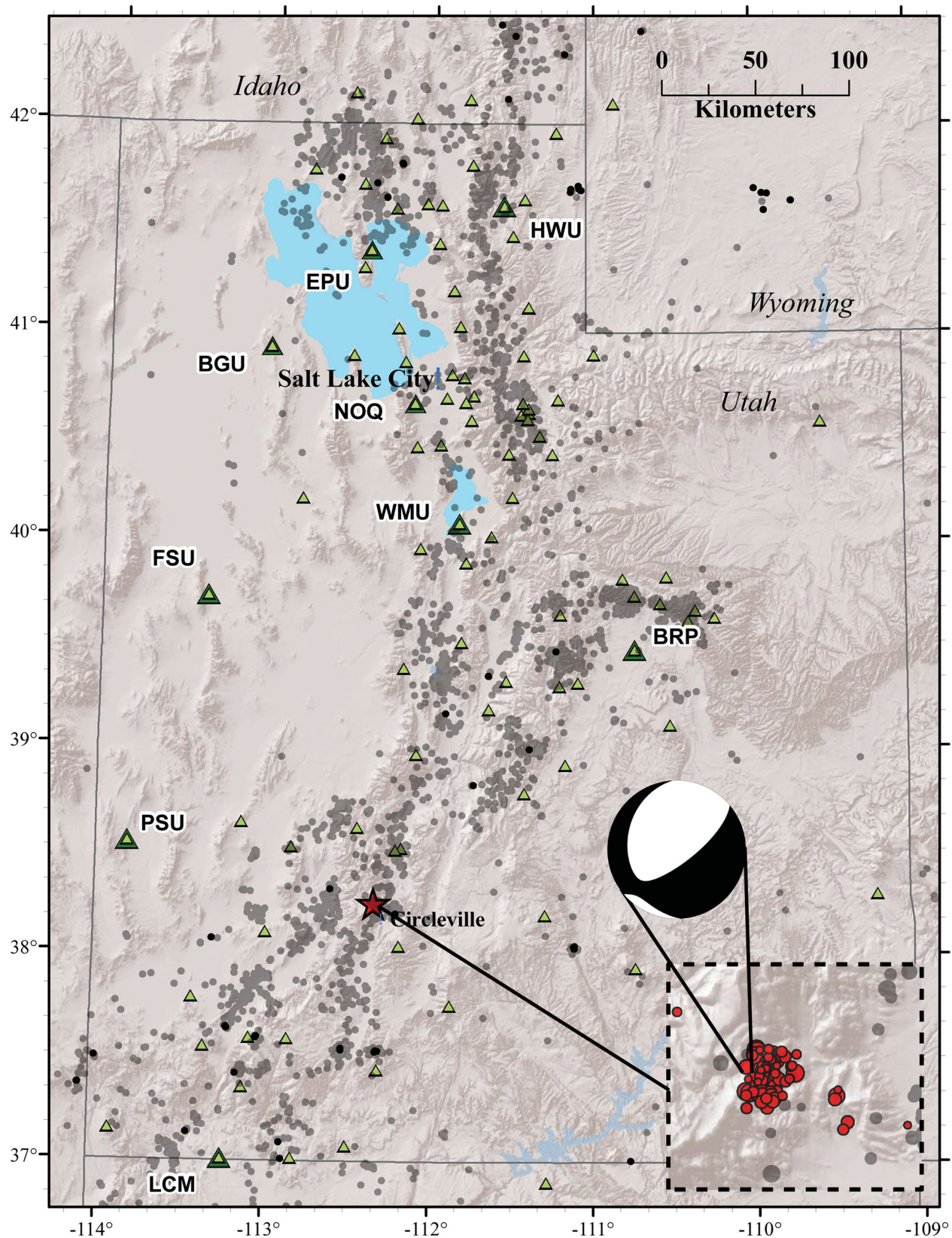


Figure 2. Map of the study area showing the location of the 2011 January 3 Circleville earthquake (red star), the locations of infrasound arrays (green triangles), seismic stations in the Utah regional network (open triangles) and background seismicity from the UU seismic catalogue from 2006 May to 2011 June (grey and black dots, where black dots denote events above M_w 3.0). The inset shows a zoom on the earthquake epicentre and includes the locations of aftershocks (red circles).

Infrasound data analysis

Epicentral infrasound from the 2011 January 3 Circleville earthquake was observed at six infrasound arrays located towards the north of the epicentre—with increasing distance these are BRP, WMU, NOQ, BGU, EPU and HWU (Fig. 3). In addition, secondary infrasound was observed at the three remaining arrays (PSU, LCM and FSU—which missed the epicentral infrasound), and possibly at BGU, BRP and EPU. At PSU, secondary infrasound peaks at ~12:20:00 (after the time window for epicentral infrasound), with an azimuthal deviation of 3.25° from the epicentre. At LCM, secondary infrasound peaks at 12:20:10 (also after the time window for epicentral infrasound), with an azimuthal deviation of 9.1°. In contrast to PSU and LCM, the secondary arrival at FSU arrives early (peaking at 12:13:20), with a very small azimuthal deviation of 0.35°. A detailed analysis of the origin of secondary infrasound arrivals is beyond the scope of this paper.

The focus of this paper is on the epicentral infrasound arrivals, summarized in Table 1. For each of these measurements, the signal occurred clearly within the epicentral arrival window (a time

window defined relative to the origin time and bounded by group velocities of 0.34 km s⁻¹, representing the fastest possible velocity associated with a direct wave, and 0.22 km s⁻¹, representing the slowest possible velocity associated with a wave that is refracted in the thermosphere). To locate the source associated with these signals, the data were processed using the InfraMonitor package (Arrowsmith & Whitaker 2008). We filtered the data from 1 to 5 Hz using a four-pole Butterworth filter to enhance the signal-to-noise ratio. Next, detections were obtained automatically using an adaptive F-detector (Arrowsmith *et al.* 2009b) and confirmed by analyst review. The detections at each array were associated and located using the Bayesian Infrasound Source Locator (BISL; Modrak *et al.* 2010). The subsequent event location uncertainty polygon (Fig. 4) is consistent with an infrasound source located at the epicentre. We note that the localization solution shown in Fig. 4 does not account for wind bias and the solution is offset slightly from the epicentre.

To investigate the reason why epicentral infrasound from the earthquake was not detected at the three closest stations (LCM, PSU and FSU—located to the west of the epicentre) while being observed at the six other stations, we performed simulations using a

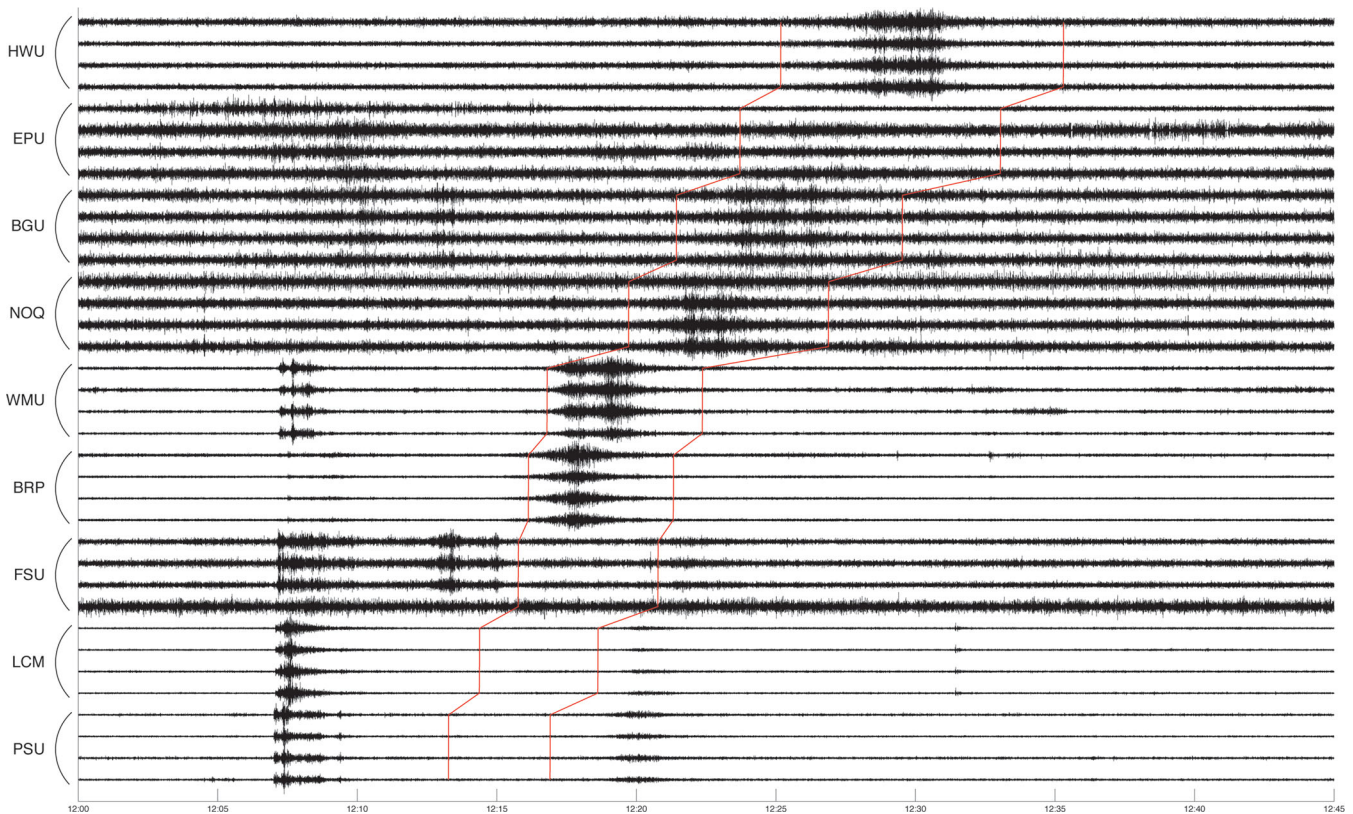


Figure 3. Filtered waveforms (Butterworth 4-pole filter from 1 to 5 Hz) for all nine arrays, ordered by epicentral distance (the earthquake was not detected at the closest three sites). Red lines denote group velocities of 0.34 and 0.22 km s⁻¹. Times represent UTC time.

Table 1. A summary of infrasound observations from the Circleville earthquake. Cross-correlation estimates represent average pairwise cross-correlations in the processing time window between each pair of elements at each array. *A*_{max} denotes the maximum peak-to-peak amplitude in Pascals.

Array	Distance (km)	Group velocity at <i>A</i> _{max} (km s ⁻¹)	Azimuthal deviation at <i>A</i> _{max} (°)	Period at <i>A</i> _{max} (s)	Cross-correlation at <i>A</i> _{max}	<i>A</i> _{max} (Pa)
BRP	194.3	0.29	1.3	0.30	0.91	0.110
WMU	208.4	0.27	6.0	0.68	0.92	0.060
NOQ	268.2	0.27	-6.1	0.41	0.47	0.089
BGU	303.1	0.27	-5.7	0.39	0.68	0.019
EPU	349.5	0.30	-8.2	0.30	0.49	0.024
HWU	379.4	0.26	-1.2	0.60	0.87	0.023

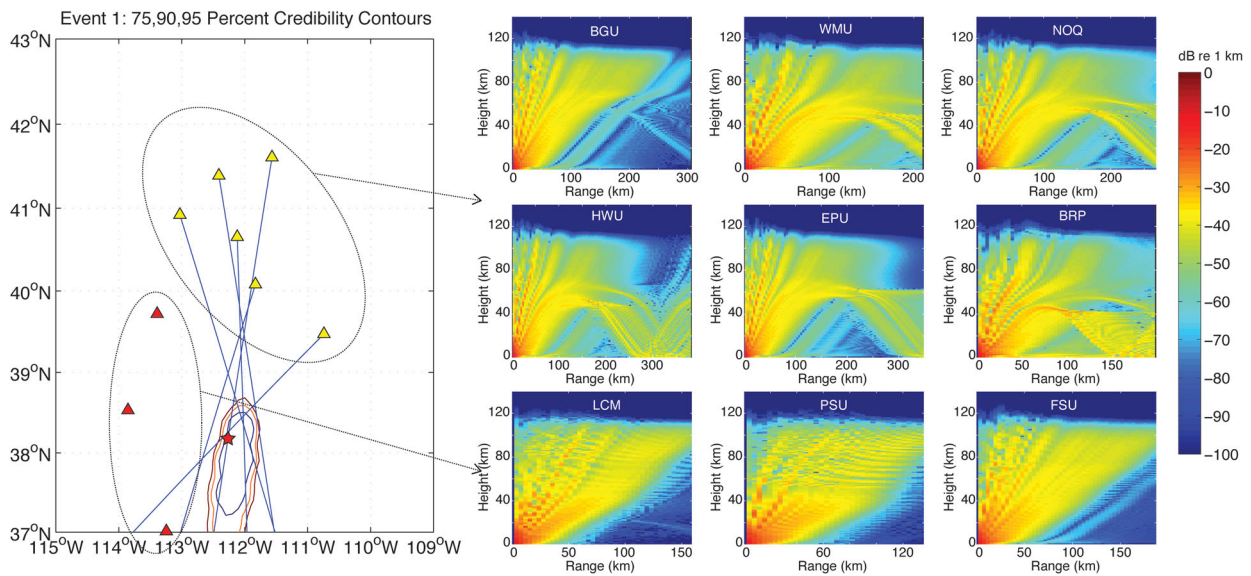


Figure 4. The bearings and arrival times of infrasound recorded at the six arrays to the north (yellow triangles) is consistent with an epicentral infrasound source (the seismic location is shown by the red star, location contours represent 75, 90 and 95 per cent credibility contours for the infrasound location). The absence of detections at the three arrays to the west (red triangles) is not inconsistent with this hypothesis: Parabolic Equation modelling of infrasound propagation (right panel) from the epicentre location towards each array does not predict ducting of infrasound towards the west. PE modelling was performed using the Ground-to-Space Model (Drob *et al.* 2003) to the nearest hour. The bottom right of each simulation represents the corresponding station location.

Parabolic Equation (PE) propagation model (West *et al.* 1992) and the Ground-to-Space (G2S) atmospheric model (Drob *et al.* 2003) extracted for 12:00 UT. For a suite of simulations at frequencies ranging from 1 to 5 Hz, no ducting of energy was predicted to the three closest arrays whereas ducts (albeit a weak duct for BGU) were predicted to the remaining six arrays (Fig. 4). Thus, the absence of an arrival at LCM, PSU and FSU is not inconsistent with an infrasound source located at the epicentre.

Studies of secondary infrasound have either noted large backazimuth variations associated with the passage of Rayleigh waves through mountainous regions (Le Pichon *et al.* 2003), or backazimuths associated with certain peaks (Arrowsmith *et al.* 2009a). In contrast, for Circleville, at six of the arrays, we observe discrete arrivals with consistent backazimuths that point back to the epicentre region, and with arrival times that occur within the time window predicted for infrasound from an epicentral source (red lines in Fig. 3). These signal characteristics strongly suggest an epicentral infrasound source. In the next section, we further explore this hypothesis by modelling the infrasound source at the epicentre as constrained by the seismic observations, allowing us to assess whether or not the signals are consistent with such a source model.

Modelling the epicentral infrasound source

We use a coupled (seismic and acoustic) numerical source model to investigate the generation of infrasound from earthquakes. The coupled model fuses a 3-D finite difference time domain algorithm (Larsen & Schultz 1995) that computes near-source ground motions from the earthquake with a Rayleigh integral technique to calculate the near-field acoustic pressure. We note that Green *et al.* (2009) used a similar technique for modelling the near-field acoustic pressure from the 2007 April 28 Folkestone earthquake, calculating the radiation from sea cliffs in the vicinity of the earthquake. In contrast, here we model the radiation from a flat surface over the earthquake epicentre, showing that the measured signals are con-

sistent with ground motion coupling directly above the hypocentre. Far-field acoustic pressures are subsequently obtained using a time domain Parabolic Equation (TDPE) technique (Whitaker & Norris 2008). The far-field acoustic pressures predicted at each array can then be compared with the pressure waveforms observed at the six arrays in this example.

The seismic component of the modelling uses the moment tensor solution obtained by UU (refer to the Seismic analysis section), the depth of 8 km estimated from the moment tensor solution, a source time function consisting of a Gaussian with a half-width at half-height of 0.5 s, and a slightly modified (the velocity in the upper most layer was reduced) 1-D geological model used by UU for earthquake location in Southern Utah (modified from Keller *et al.* 1975). A flat earth is assumed and vertical component seismograms are calculated on a 2-D surface grid centred on the epicentre (with dimensions of $40 \text{ km}^2 \times 40 \text{ km}^2$, and grid node spacing of 1 km in both X and Y). We use the ELAS-3D code (Larsen & Schultz 1995), which is an explicit 2-D/3-D elastic finite-difference wave propagation code based on the elastodynamic formulation of the wave equation on a staggered grid. The ELAS-3D code has been used in a number of previous studies for modelling broad-band seismic waveforms from earthquakes (Hartzel *et al.* 1999; Dolenc *et al.* 2005; Day *et al.* 2008). To satisfy the Courant condition and stability for the frequency content of the source, the model has a grid spacing of 50 m and a time step of 0.0032 s. To avoid effects from the absorbing boundaries on the seismometer grid, the model grid extends 5 km beyond the seismometer grid in each direction, and also extends 12 km below the source.

Although ELAS-3D is used to calculate waveforms at the free surface, the waveform amplitudes are scaled using the peak horizontal ground motions determined in the ShakeMap calculations (refer to the Seismic analysis section). The purpose for scaling the waveforms is twofold. First, the ELAS-3D code does not account for absolute seismic moment. Second, the sensitivity to the specific (but poorly constrained) surface velocity structure in the modelling, which dominates the surface accelerations, is reduced. ELAS-3D

thus provides us with the acceleration time history and relative amplitudes, but not with absolute amplitudes. Finally, before using the simulation results for Rayleigh integral modelling, the scaled 2-D acceleration–time functions are interpolated onto a finer grid spacing of 100 m × 100 m using splines and scaled by 75 per cent to account for differences between horizontal and vertical components of motion (the empirical site amplification terms are for horizontal components only). The PZA’s over all times as a function of location around the epicentre from this methodology are plotted in Fig. 5.

As discussed in detail in Blackstock (2000), the Rayleigh integral can be used to calculate the acoustic pressure at some distance from a baffled piston (i.e. all acoustic radiation is constrained to propagate in the forward direction) as an integral of contributions from accelerations of all infinitesimal area elements, dS , of the piston

$$p(x, y, z; t) = \rho_0 \int_S \frac{\dot{u}_p(x', y'; t - R/c_0)}{2\pi R} dS,$$

where x', y' are the coordinates of the source point on the piston, R is the distance to the field point of interest, ρ_0 is the air density and c_0 is the speed of sound in air.

The Rayleigh integral is an approximation to the Helmholtz–Kirchoff integral theorem and is strictly valid in the far field, beyond the Rayleigh distance, defined in general by

$$R_0 \equiv \frac{S}{\lambda},$$

where S is the surface area of the piston and λ is the wavelength. This limitation imposes a constraint on the area of the piston that can be modelled, because the assumption of a constant sound speed— c_0 in the Rayleigh integral—becomes unrealistic at large distances from the source due to the variation of temperature and winds with height (temperature typically decreases in the troposphere and mesosphere, and increases in the stratosphere and thermosphere;

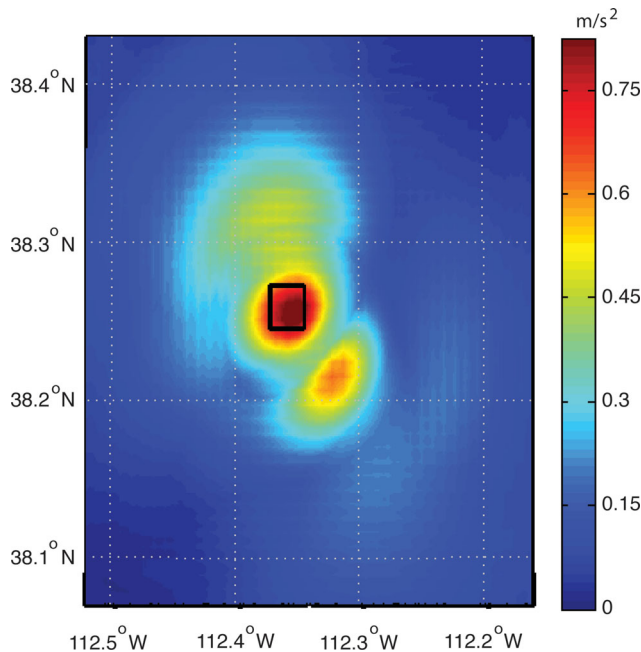


Figure 5. Map showing the peak vertical accelerations (in m s^{-2}) as a function of location. The black box denotes the subregion, centred on the maximum acceleration, which is used for the Rayleigh Integral modelling.

winds are strongest in the jet stream and stratospheric jet—see Arrowsmith *et al.* 2010). As long as we restrict the Rayleigh integral modelling to low altitudes, the assumption of a uniform sound speed is reasonable.

We have performed a series of synthetic calculations using different piston areas, and find that the far-field approximation is appropriate at 5 km elevation from a $3 \times 3 \text{ km}^2$ region (Fig. S1). There is a trade-off between the area of the piston (ideally we would choose the maximum possible area to model as much of the source region as possible) and the elevation at which the Rayleigh integral is calculated (ideally we would choose the minimum elevation to minimize errors associated with the constant sound speed approximation), whereby increasing the piston area requires us to increase the elevation. We find that a $3 \times 3 \text{ km}^2$ region centred on the location of peak acceleration (black box in Fig. 5) captures the peak accelerations, whereas an elevation of 5 km is typically below any significant variations in temperature and wind.

We implement the Rayleigh integral by summing over the contributions of each individual $0.1 \times 0.1 \text{ km}^2$ region within the full $3 \times 3 \text{ km}^2$ region. This approach enables us to properly account for differences in phasing and amplitude at different locations. We note that the contribution of each element appropriately accounts for the observation position relative to that element (i.e. the ‘directivity’ of each element is accounted for in calculating the far-field pressure). The resultant acoustic pressure at 5 km directly above the peak acceleration (Fig. 6a) represents the predicted pressure on-axis. Although a peak acoustic pressure of $\sim 150 \text{ Pa}$ may intuitively seem rather high for an underground source, it is not inconsistent with measurements from underground nuclear tests. To provide an example of an underground event recorded on axis, a peak-to-peak acoustic pressure of 500 Pa was recorded by aircraft at an elevation of 8.64 km above the Rummy test (a $M_s = 4.1$ event conducted at Yucca Flat on 1978 September 27; Banister & Hereford 1982). The Rayleigh integral was used to model the pressure recorded from this event and found to agree well with the predictions (Banister & Hereford 1982).

To account for differences in the on-axis source term, and the source term propagated into the far field, we must account for the radiation pattern. The acoustic radiation pattern can be represented by an amplitude directivity factor, D , which is defined as the pressure at any angle θ relative to the pressure (at the same range r) at $\theta = 0$

$$D(\theta) = \frac{P(r, \theta)}{P(r, 0)}.$$

Following Blackstock (2000), by assuming that the whole $3 \times 3 \text{ km}^2$ region acts as a single piston, we can approximate the radiation pattern from a circular piston of radius a as

$$D(\theta) = \frac{2J_1(ka \sin \theta)}{ka \sin \theta},$$

where J_1 is the first-order Bessel function of the first kind, k is the wavenumber ($k = 2\pi/\lambda$), and θ is the angle from the zenith. A more rigorous approach to handle directivity effects would be to numerically evaluate the Rayleigh integral for different launch angles; however, because the acceleration–time function is poorly characterized spatially, we believe that our simple/fast approach is suitable for this assessment. The number of nulls and secondary maxima in the radiation pattern is determined by the size of ka . As the piston size increases, relative to the wavelength, the number of nulls increases. Fig. 6(b) shows the resultant radiation pattern for a circular piston of diameter 3 km and frequency of 1 Hz

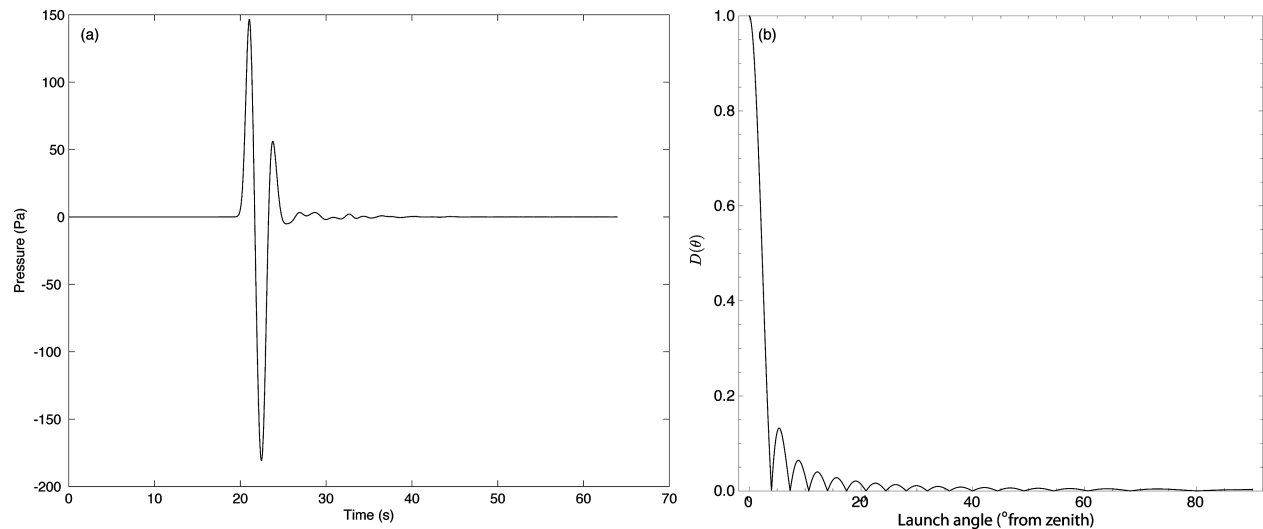


Figure 6. Near-source acoustic modelling. By summing the contributions due to all the $0.1 \text{ km}^2 \times 0.1 \text{ km}^2$ cells within a $3 \text{ km}^2 \times 3 \text{ km}^2$ region centred on the peak ground acceleration (Fig. 5), we compute the near-field acoustic source term directly above the centre of the grid using the Rayleigh integral. The radiation pattern can be used to scale this source term based on the launch angle.

(approximating our source). We note that, although the sidelobes are artefacts of the piston area and wave frequency, the amplitudes of $D(\theta)$ relevant to our problem—discussed below—are not strongly dependent on these values.

We performed ray tracing using the Tau-P method (Garces *et al.* 1998; Drob *et al.* 2010) and the G2S atmospheric model for the Circleville epicentre location at 12:00 UT to obtain the ‘minimum’ launch angle (from the zenith) required to obtain a ray that returns to the ground. This allows us to estimate the ‘maximum’ value of $D(\theta)$ that should be used for scaling the source function in Fig. 6(a). We choose the maximum value to estimate the largest expected acoustic pressure at the receiver due to our modelled epicentral infrasound source. By shooting a suite of rays with different launch angles at an azimuth of 0° (the observations are all towards the north), the minimum launch angle from the zenith required to obtain a return is 52° (Fig. S2). Using the radiation pattern plotted in Fig. 6(b), this corresponds to a maximum value of $D(\theta)$ equal to 0.005.

After scaling the synthetic near-source acoustic pressure by 0.005 to account for these radiation effects, we propagate this source term through the G2S model to each array using a TDPE technique (Whitaker & Norris 2008). The TDPE technique uses Fourier synthesis to derive the received waveform by combining simulations from a continuous wave PE in multiple frequency bins. We synthesize frequencies from 0 to 3 Hz to capture the dominant frequency component in the recorded waveforms. The TDPE simulations are calculated relative to a reference range of 5 km, which is the altitude at which we compute the near-field acoustic pressure. Gravity wave perturbations are incorporated into the G2S model using Gardner’s gravity wave model (Norris & Gibson 2002). We have run a series of simulations with different gravity wave realizations, finding that the main arrivals are consistent, whereas arrivals associated with weak ducts may come and go. A comparison between the observations and predictions from one such simulation is shown in Fig. 7. Overall, the agreement between observations and predictions is remarkable. In particular, the predicted and observed amplitudes are within a factor of 2 (on average, the synthetic amplitudes are a factor of 1.6 larger than the observed amplitudes). In addition, arrivals are predicted at all six arrays where signals are observed, and importantly not predicted at the remaining three arrays. In some cases, duration

is also well predicted (e.g. HWU and WMU) whereas in other cases it is not predicted well (e.g., BRP and NOQ). Due to strong ducts along the source–receiver paths, these broad conclusions are robust for every gravity wave realization that we have run. We note that the synthetics are far more impulsive than the observations, and in some cases show more than one distinct arrivals when the observations show only one packet of energy. Recent work on modelling infrasound from explosions at similar distances to this study (corresponding to a single stratospheric bounce) have found that the inclusion of gravity waves does not always result in the temporal smearing of energy that is observed (R. Gibson, personal communication, 2011), suggesting that propagation effects may contribute to these differences. However, our source model also makes a number of simplifying assumptions that may contribute to these differences (see the discussion in the next section for further details on this).

DISCUSSION AND CONCLUSIONS

The high-density infrasound measurements of the 2011 January 3 Circleville earthquake provide a unique opportunity to explore models for the generation of infrasound from earthquakes. The observed infrasound signals at six arrays occur within the epicentral time window and have backazimuths that do not change significantly with time and are consistent with a source location at the epicentre. Based on these observations, our working hypothesis is that the infrasound was generated by surface pumping in the epicentre region. Although three arrays located to the west of the epicentre do not observe epicentral infrasound, the absence of a signal at these arrays is not inconsistent with our hypothesis because state-of-the-art atmospheric models do not predict a path for energy from the epicentre region to those arrays.

By modelling the source region as a baffled piston, the major conclusion of this paper is that the observations are consistent with this simple model. Our baffled piston model incorporates information on the source mechanism, depth, local geology, near-source radiation pattern and atmospheric temperatures and winds that affect the propagation of infrasound into the far field. However, in

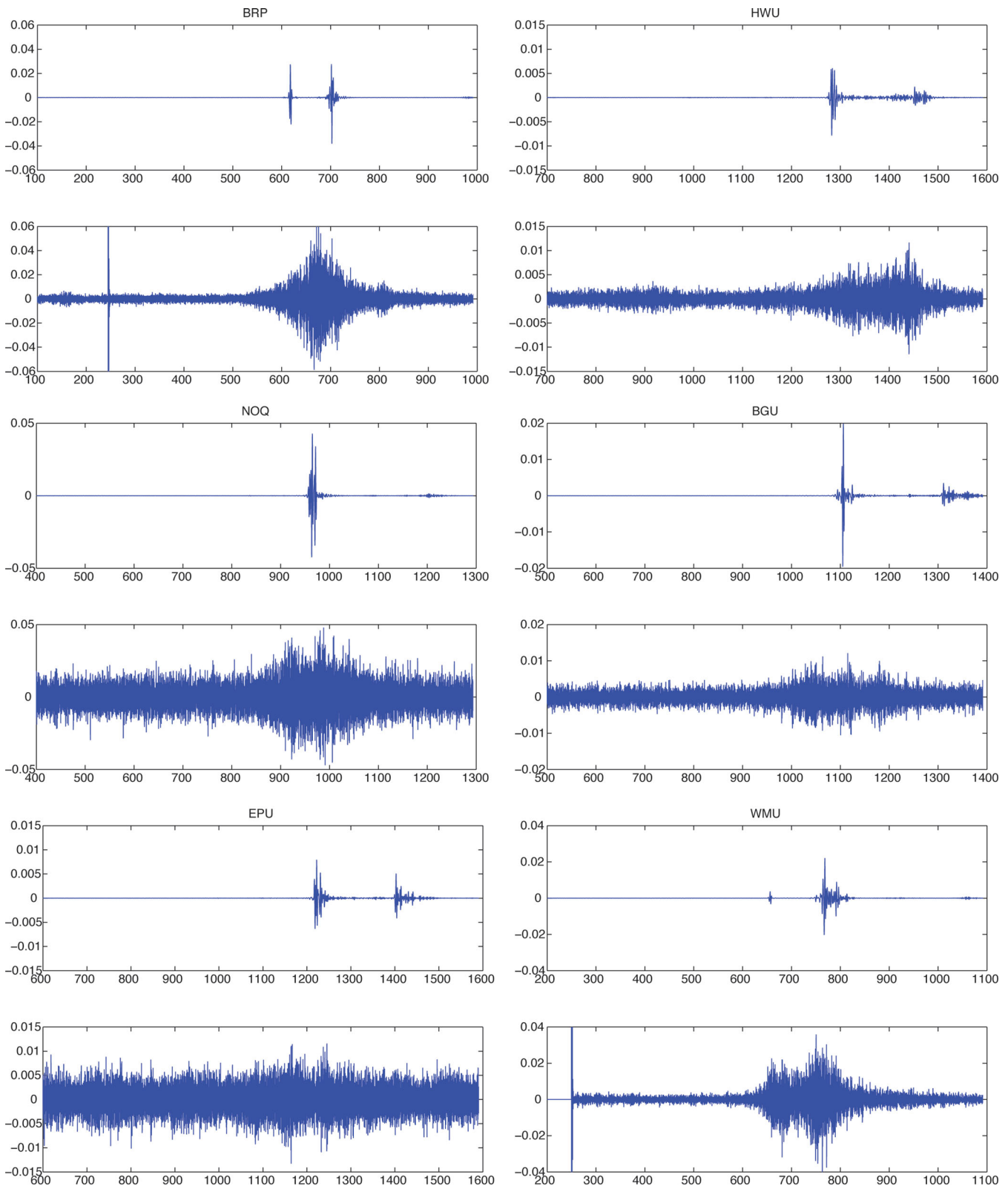


Figure 7. Comparison between the predicted (top panel for each pair) and observed (bottom panel for each pair) infrasound at the six arrays that detected the Circleville earthquake. Note that, in all cases, the predicted and observed waveforms are plotted on the same time and amplitude scales.

contrast to previous models of infrasound from earthquakes, our model assumes a flat earth. Lacking any near-field measurements, we must rely upon the agreement between far-field observations and predictions. However, the near-field acoustic pressure is con-

sistent in amplitude with aircraft measurements of similar seismic magnitude underground nuclear tests.

We do not claim that our baffled piston model can uniquely explain the observations—shaking of topography may indeed play

an important role. Indeed, the epicentral area has significant relief. The epicentre itself projects to the crest of a local high. Over a kilometre in the horizontal direction, the relief is $\sim 300\text{m}$ very sharp to the southeast (consistent with a normal fault dipping to the southeast). Nevertheless, the fact that our modelled results fit the observations sufficiently well in terms of amplitude indicates that topographic effects above the hypocentre may be secondary in importance. This study motivates the need for more high-density observations of infrasound from earthquakes to validate different models for the generation of infrasound from earthquakes, and to understand what factors may cause one mechanism to dominate. In parallel with these efforts, further research is needed to improve the modelling approach used in this study. A number of simplifying assumptions were made in this study, both in computing the source term and accounting for propagation effects, which likely contributes to the differences between the observations and predictions. The most significant assumptions, which merit further study, include

- (i) The flat-earth assumption. The lack of topography in our source model may increase the acoustic source duration.
- (ii) A simple 1-D geological model. Our seismic velocity model assumes flat layers.
- (iii) We did not include a finite fault model or incorporate attenuation in the solid earth model.
- (iv) The near-field acoustic pressure is only calculated for a $3\text{ km}^2 \times 3\text{ km}^2$ region, instead of summing over the full region, which requires a more sophisticated numerical approach such as the full Kirchhoff–Helmholtz integral (Pierce 1981).
- (v) The Rayleigh integral assumes a constant sound speed.
- (vi) The time-domain PE neglects backscatter and does not account for possible non-linear propagation effects.
- (vii) The atmospheric model is smooth, acoustic gravity waves are incorporated using a spectral model and turbulence is not accounted for.

Ultimately, it is hoped that enhancements to models for the generation of infrasound from earthquakes will lead to improvements in existing scaling relations by enabling us to separate the effects of different source effects, such as depth and focal mechanism.

ACKNOWLEDGMENTS

We are grateful to Alexis Le Pichon for providing the data in Fig. 1 and for providing helpful comments on this research. We also thank Mark Hale for his contributions to this paper. We thank the editor, Ingo Grevemeyer, and two anonymous reviewers for their comments, which helped improve this manuscript. The InfraMap toolbox was used for TDPE modelling. The authors acknowledge the support of Leslie A. Casey and the National Nuclear Security Administration Office of Non-proliferation Research and Development for funding this work. This work was completed under the auspices of the U.S. Department of Energy by Los Alamos National Laboratory, the University of Utah and Southern Methodist University under contracts LA09-Depth-NDD02, LA09-BAA09-NDD02 and DE-AR52-09NA29325.

REFERENCES

Abrahamson, N.A. & Shedlock, K.M., 1997. Overview (special issue on Ground Motion Attenuation Relationships), *Seism. Res. Lett.*, **68**, 9–23.

- Arrowsmith, S.J. & Whitaker, R.W., 2008. InfraMonitor: a tool for regional infrasound monitoring, in *Proceedings of the 30th Monitoring Research Review*, Portsmouth, Virginia.
- Arrowsmith, S.J. *et al.*, 2008. Regional monitoring of infrasound events using multiple arrays: application to Utah and Washington State, *Geophys. J. Int.*, **175**, 291–300.
- Arrowsmith, S.J., Burlacu, R., Whitaker, R.W. & Randall, R., 2009a. A repeating secondary source of infrasound from the Wells, Nevada earthquake sequence, *Geophys. Res. Lett.*, **36**, doi:10.1029/2009GL038363.
- Arrowsmith, S.J., Whitaker, R.W., Katz, C. & Hayward, C., 2009b. The F-detector revisited: an improved strategy for signal detection at seismic and infrasound arrays, *Bull. seism. Soc. Am.*, **99**, 449–453.
- Arrowsmith, S.J., Johnson, J.B., Drob, D.P. & Hedlin, M.A.H., 2010. The seismo-acoustic wavefield: a new paradigm in studying geophysical phenomena, *Rev. Geophys.*, **48**, doi:10.1029/2010RG000335.
- Banister, J.R. & Hereford, W.V., 1982. *Rummy High Altitude Pressure Measurements and Analysis*, Sandia National Laboratories, Albuquerque, New Mexico.
- Benioff, H. & Gutenberg, B., 1939. Observations with electromagnetic microbarographs, *Nature*, **144**, 478, doi:10.1038/144478a0.
- Blackstock, D.T., 2000. *Fundamentals of Physical Acoustics*, p. 541, John Wiley and Sons, New York.
- Bolt, B.A., 1964. Seismic air waves from the great 1946 Alaskan earthquake, *Nature*, **6937**, 1095–1096.
- Borcherdt, R.D., 1994. Estimates of site-dependent response spectra for design (Methodology and Justification), *Earthq. Spectra*, **10**, 617–653.
- Cook, R.K., 1971. Infrasound radiated during the Montana earthquake of 1959 August 18, *Geophys. J. R. astr. Soc.*, **26**, 191–198.
- Day, S.M., Graves, R., Bielak, J., Dreger, D., Larsen, S., Olsen, K.B., Pitarka, A. & Ramirez-Guzman, L., 2008. Model for basin effects on long-period response spectra in Southern California, *Earthq. Spectra*, **24**, 257–277, doi:10.1193/1.2857545.
- Dolenc, D., Dreger, D. & Larsen, S., 2005. Basin Structure influences on the propagation of teleseismic waves in the Santa Clara Valley, California, *Bull. seism. Soc. Am.*, **95**, 1120–1136. doi:10.1785/0120040059.
- Donn, W.L. & Posmentier, E.S., 1964. Ground-coupled air waves from the great Alaskan earthquake, *J. geophys. Res.*, **69**, 5357–5361.
- Drob, D.P., Garces, M., Hedlin, M.A.H. & Brachet, N., 2010. The temporal morphology of infrasound propagation, *Pure appl. Geophys.*, **167**, doi:10.1007/s00024-010-0080-6.
- Drob, D.P., Picone, J.M. & Garces, M., 2003. Global morphology of infrasound propagation, *J. geophys. Res.*, **108**, doi:10.1029/2002JD003307.
- Garces, M., Hansen, R.A. & Lindquist, K.G., 1998. Traveltimes for infrasonic waves propagating in a stratified atmosphere, *Geophys. J. Int.*, **135**, 255–263.
- Gomberg, J.S., Shedlock, K.M. & Roecker, S.W., 1990. The effect of S-wave arrival times on the accuracy of hypocenter estimation, *Bull. seism. Soc. Am.*, **80**, 1605–1628.
- Green, D.N., Guilbert, J., Le Pichon, A., Sebe, O. & Bowers, D., 2009. Modelling ground-to-air coupling for the shallow ML 4.3 Folkestone, United Kingdom, earthquake of 28 April 2007, *Bull. seism. Soc. Am.*, **99**, 2541–2551, doi:10.1785/0120080236.
- Hartzel, S., Harmsen, S., Frankel, A. & Larsen, S., 1999. Calculation of broadband time histories of ground motion: comparison of methods and validation using strong-ground motion from the 1994 Northridge earthquake, *Bull. seism. Soc. Am.*, **89**, 1484–1504.
- Hermann, R.B., Benz, H. & Ammon, C.J., 2011. Monitoring the earthquake source process in North America, *Bull. seism. Soc. Am.*, **101**, doi:10.1785/0120110095.
- Keller, G.R., Smith, R.B. & Braile, L.R., 1975. Crustal structure along the Great Basin Colorado Plateau transition from seismic refraction studies, *J. geophys. Res.*, **80**, 1093–1098.
- Kim, T.S., Hayward, C. & Stump, B., 2004. Local infrasound signals from the Tokachi-Oki earthquake, *Geophys. Res. Lett.*, **31**, doi:10.1029/2004GL021178.
- Larsen, S. & Schultz, C.A., 1995. *ELAS3D: 2D/3D Elastic Finite-Difference Wave Propagation Code*, Lawrence Livermore National Laboratory, Livermore, CA.

- Le Pichon, A., Guilbert, J., Vega, A., Garces, M. & Brachet, N., 2002. Ground-coupled air waves and diffracted infrasound from the Arequipa earthquake of June 23, 2001, *Geophys. Res. Lett.*, **29**, doi:10.1029/2002GL015052.
- Le Pichon, A., Guilbert, J., Vallee, M., Dessa, J.X. & Ulziibat, M., 2003. Infrasonic imaging of the Kunlun Mountains for the great 2001 China earthquake, *Geophys. Res. Lett.*, **30**, doi:10.1029/2003GL017581.
- Le Pichon, A., Herry, P., Mialle, P., Vergoz, J., Brachet, N., Garces, M., Drob, D.P. & Ceranna, L., 2005. Infrasound associated with 2004–2005 large Sumatra earthquakes and tsunami, *Geophys. Res. Lett.*, **32**, doi:10.1029/2005GL023893.
- Mikumo, R., 1968. Atmospheric pressure waves and tectonic deformation associated with the Alaskan earthquake of March 28, 1964, *J. geophys. Res.*, **73**, 2009–2025.
- Modrak, R.T., Arrowsmith, S.J. & Anderson, D.N., 2010. A Bayesian framework for infrasound location, *Geophys. J. Int.*, **181**, 399–405, doi:10.1111/j.1365-246X.2010.04499.x.
- Mutschlecner, J.P. & Whitaker, R.W., 2005. Infrasound from earthquakes, *J. geophys. Res.*, **110**, doi:10.1029/2004JD005067.
- Norris, D. & Gibson, R., 2002. InfrMAP enhancements: environmental/propagation variability and localization accuracy of infrasonic networks, in *Proceedings of the 24th Seismic Research Review*, Ponte Vedra Beach, FL, pp. 809–813.
- Pierce, A.D., 1981. *Acoustics: An Introduction to Its Physical Principles and Applications*, McGraw-Hill, Inc., New York, NY.
- Stump, B. et al., 2007. *Seismic and Infrasound Energy Generation and Propagation at Local and Regional Distances: Phase I – Divine Strake Experiment*, Air Force Research Laboratory, Albuquerque, NM.
- Wald, D.J., Worden, B.C., Quitoriano, V. & Pankow, K.L., 2003. *ShakeMap Manual: Technical Manual, User's Guide, and Software Guide*, Techniques and Methods 12-A1, USGS, Golden, CO, 132pp.
- West, M., Gilbert, K.E. & Sack, R.A., 1992. A tutorial on the Parabolic

Equation (PE) Model used for long range sound propagation in the atmosphere, *Appl. Acoust.*, **37**, 31–49.

- Whidden, K., Pankow, K.L. & Taira, T., 2011. A catalog of regional moment tensors in Utah, *Seism. Res. Lett.*, **82**, 295.
- Whitaker, R.W. & Norris, D.E., 2008. Infrasound Propagation, in *Handbook of Signal Processing in Acoustics*, pp. 1497–1519, eds Havelock, D., Kuwano, S. & Vorlander, M., Springer, New York, NY.
- Young, J.M. & Greene, G.E., 1982. Anomalous infrasound generated by the Alaskan earthquake of 28 March 1964, *J. acoust. Soc. Am.*, **71**, 334–339.

SUPPORTING INFORMATION

Additional Supporting Information may be found in the online version of this article:

Figure S1. Acoustic pressure from a circular piston of radius 3 km at different heights (1–20 km in increments of 1 km) assuming a constant acceleration of 1 m s^{-2} . Above 5 km, the predicted pressure falls off as $1/r$, indicating that the far-field assumption is valid above this height.

Figure S2. TauP simulations of ray paths shot at a range of launch angles and an azimuth of 0° . The first returning ray—a thermospheric return—occurs at a launch angle of 52° from the zenith.

Please note: Wiley-Blackwell is not responsible for the content or functionality of any supporting materials supplied by the authors. Any queries (other than missing material) should be directed to the corresponding author for the article.